

Revisiting γ -Ray Orbital Modulation in the Redback Millisecond Pulsar PSR J2039–5617MENGQING ZHANG,¹ SHENGBIN PEI,¹ SHAN CHANG,¹ AND PENGFEI ZHANG¹¹*Department of Astronomy, School of Physics and Astronomy, Key Laboratory of Astroparticle Physics of Yunnan Province, Yunnan University, Kunming 650091, People's Republic of China; zhangpengfei@ynu.edu.cn***ABSTRACT**

PSR J2039–5617 is a redback millisecond pulsar binary system consisting of a compact star with a mass of 1.1–1.6 M_{\odot} and a low-mass companion of 0.15–0.22 M_{\odot} . For this binary, we performed a timing analysis using 16 years of data from the Fermi Large Area Telescope, covering the period from 2008 August to 2024 October. Our analysis detected an orbital modulation with a period of 0.2279781 days at a significance level of $\sim 4\sigma$, which is in good agreement with previous findings. However, unlike previous reports, we identified a transition in the orbital modulation around 2021 August, after which the orbital signal disappeared. We speculate that the system may be undergoing a transition from a rotation-powered to an accretion-powered state at this epoch. Additionally, we conducted the phase-resolved and spectral analyses, and in the phase-resolved results, we observed an anti-correlation between its γ -ray and X-ray emissions, which consistent with the predictions of high-energy radiation models for such systems. We provide some predictive discussions based on the results of γ -ray data analysis, and future Fermi-LAT observations will determine whether these predictions hold true.

Keywords: Gamma-ray sources(633); Millisecond pulsars (1062); Pulsars (1306); Periodic variable stars(1213)

1. INTRODUCTION

Millisecond pulsars (MSPs) are generally regarded as the rapidly rotating neutron stars that have undergone a recycling process. By accreting material from a companion star, they gain angular momentum, which accelerates their rotation and reduces their spin period to the millisecond range (Bhattacharya & van den Heuvel 1991). These pulsars are most commonly found in binary systems. Among them, two prominent subclasses of eclipsing MSP binaries are the so-called spider systems: Redbacks and Black Widows, both of which represent special categories of compact binary evolution (Roberts 2013; Chen et al. 2013).

Black Widow system typically consists of a neutron star and a very low-mass companion star, usually $< 0.05 M_{\odot}$, its orbital period is typically under 10 hours. In Black Widow, the neutron star's strong radiation and particle wind continuously strip mass from the companion star, effectively shredding it over time. The most famous example is PSR B1957+20 (Fruchter et al. 1988), which was first identified as a Black Widow system. As Black Widow, Redback systems contains a companion star with a mass ranging from 0.1 to 0.5 M_{\odot} . The orbital periods of these systems usually span from several hours

to a few days. The companion star in Redback systems is typically a low-mass main-sequence star or a slightly evolved star. A well-known example of a Redback system is PSR J1023+0038, which exhibits a remarkable behavior of transitioning between a millisecond pulsar and a low-mass X-ray binary (LMXB) state, depending on the accretion activity (Archibald et al. 2009). It is widely believed that Redback systems may be evolutionary precursors to Black Widow systems (Benvenuto et al. 2014). As the companion star in a Redback system continues to lose mass due to the pulsar's intense radiation and wind, the system could eventually evolve into a Black Widow system, with the companion becoming increasingly stripped and more negligible in mass (Alpar et al. 1982).

PSR J2039–5617 is a Redback MSP binary system with a spin period of 2.65 ms. Its γ -ray pulsations were first detected in Fermi-LAT data through a directed search performed with the Einstein@Home distributed volunteer computing system (Clark et al. 2021), and subsequent radio pulsations were reported by Corongiu et al. (2021). Prior to these discoveries, Salvetti et al. (2015) identified its orbital period of 0.2245-day from X-ray and optical observations and proposed that

the system was the counterpart of the previously unassociated γ -ray source 3FGL J2039.6–5618 detected by Fermi-LAT. Later, Ng et al. (2018, hereafter as Ng2018) analyzed Fermi-LAT observations spanning from 2008 August 4 to 2018 January 30. By applying the Rayleigh test, they found evidence for γ -ray orbital modulation between 2008 August 4 and 2015 January 18 (MJD 57,040); however, this modulation appeared to vanish afterward. They suggested that the intrabinary shock (IBS) in this system may be located closer to the pulsar, leading to a lower Lorentz factor of the pulsar wind and consequently weakening the inverse Compton (IC) radiation, rendering the orbital modulation undetectable in γ -rays. Moreover, the transition of the redback system from the rotation-powered MSP state to the accretion-powered LMXB state is crucial for understanding the evolution of compact binary systems. The disappearance of orbital modulation could signal such a transition, marking a critical phase in the evolution of these systems. If this epoch indeed represents the shift between these two states, it would offer a unique opportunity to study the evolutionary pathway connecting them. Motivated by this possibility, we have conducted a revised timing analysis using Fermi-LAT data from PSR J2039–5617.

In γ -rays, PSR J2039–5617 was first detected as an unidentified γ -ray source in the 1FGL catalog, designated 1FGL J2039.4–5621 (Abdo et al. 2010a). It was later listed as 2FGL J2039.8–5620 and 3FGL J2039.6–5618 in the 2FGL and 3FGL catalogs, respectively (Nolan et al. 2012; Acero et al. 2015). Subsequently, Salvetti et al. (2015) identified its X-ray and optical counterparts and classified it as a candidate Redback MSP. Based on 14 years of observations covering events in the 50 MeV–1 TeV, the source was reclassified as 4FGL J2039.5–5617 (Ballet et al. 2023). Here, we performed a timing analysis using \sim 16 years of γ -ray events of 4FGL J2039.5–5617 from Fermi-LAT, detecting an orbital period of 0.2279781 days with a significance of $\sim 4\sigma$. This period is consistent with the orbital parameters reported in the pulsar ephemerides of Clark et al. (2021), Corongiu et al. (2021), and Corbet et al. (2022). Moreover, we found that its γ -ray orbital modulation persisted steadily from 2008 August 4 to 2021 August 1, rather than ceasing in 2015 January 18 as reported by Ng2018. The duration of the orbital period signal observed in the Fermi-LAT data has increased twofold. The detailed data processing is described in Section 2, followed by a summary and discussion in Section 3. The following numbers in parentheses represent the errors associated with the last digit of the parameter values.

Table 1. Best-fit results from likelihood analysis

Model	Parameter values				
	γ	d	TS	F_{ph}	
PLE4	1.89(4)	0.32(4)	2818.74	1.61(10)	Whole
	1.87(4)	0.35(4)	2202.67	1.52(11)	P_1
	2.00(7)	0.20(6)	638.30	2.07(28)	P_2
	1.93(5)	0.37(6)	1693.29	1.92(16)	Ph_{ic}
	1.79(8)	0.29(7)	632.859	1.05(15)	Ph_{sc}

Notes. Best-fit parameters of the likelihood, with F_{ph} in units of $\times 10^{-8}$ photons $\text{cm}^{-2} \text{s}^{-1}$. The parameters E_0 and b for the PLE4 model is fixed at ~ 1.10 GeV and 2/3, respectively.

2. DATA ANALYSIS AND RESULTS

2.1. Data Reduction And Best-fit Results

We selected Pass 8 Front+Back events with `evclass = 128` and `evtype = 3` within the energy range of 0.1–500.0 GeV, centered on 4FGL J2039.5–5617 (R.A. = $309^\circ.8974$ and Decl. = $-56^\circ.2836$) and covering a $20^\circ \times 20^\circ$ region of interest. The observation period spans from 2008 August 4 to 2024 October 23 (MJD 54682.687–60606.955). Events with zenith angles greater than 90° were excluded, and only high-quality events from good time intervals were retained using the filter condition “`DATA_QUAL > 0 && LAT_CONFIG==1`”. The diffuse γ -ray emissions from the Galactic and extragalactic isotropic components were modeled using the templates `gll_iem_v07.fits` and `iso_P8R3_SOURCE_V2_v1.txt`, respectively. This data reduction and analysis were conducted using Fermi tools version 2.2.0.

In the 4FGL, 4FGL J2039.5–5617’s γ -ray spectral shape is represented with a new subexponentially cut-off power-law (PLE4). Using 16 yr data, we updated its parameters by performing a binned maximum likelihood analysis based on a model file from 4FGL. The best-fit parameters were saved in an updated model file. To identify significant potential γ -ray sources not included in 4FGL, we generated a test statistic (TS) map of γ -ray residuals after excluding emissions from all 4FGL sources in the model. The residual map revealed several new, relatively significant γ -ray excesses. To account for these excesses, we iteratively added new γ -ray point sources (NGSs), with spectral shape of PowerLaw, to the model file and ultimately identified six additional sources. Their γ -ray positions were determined using `gtfindsrc`. We then re-performed the data analysis to update the model and saved the results as a best-fit model file. Based on this model, we gener-

Table 2. Additional γ -ray point sources with their results

New γ -ray sources	Coordinate (error) ^a		d^b [radian]	Γ	TS	F_γ^c
	R.A.	Dec.				
NGS ₁	308.147	-51.870 (0.065)	4.533	2.12(20)	38.83	6.30 ± 1.10
NGS ₂	302.978	-56.727 (0.044)	3.841	2.45(16)	32.24	3.19 ± 0.99
NGS ₃	310.749	-57.936 (0.003)	1.714	1.64(14)	41.89	0.32 ± 0.17
NGS ₄	302.506	-59.742 (0.031)	5.217	2.11(20)	21.16	1.09 ± 0.59
NGS ₅	304.726	-53.316 (0.034)	4.205	2.21(15)	27.87	1.86 ± 0.70
NGS ₆	307.584	-53.696 (0.191)	2.909	2.13(23)	11.22	0.92 ± 0.60

Notes. (a) Coordinates (J2000) and positional uncertainties of the six nearby NGSs, obtained using the tool *gtfindsrc*. (b) Angular distances of the six NGSs from the target source. (c) Integrated photon fluxes in 0.1–500.0 GeV with units of $\times 10^{-9}$ photons $\text{cm}^{-2} \text{ s}^{-1}$.

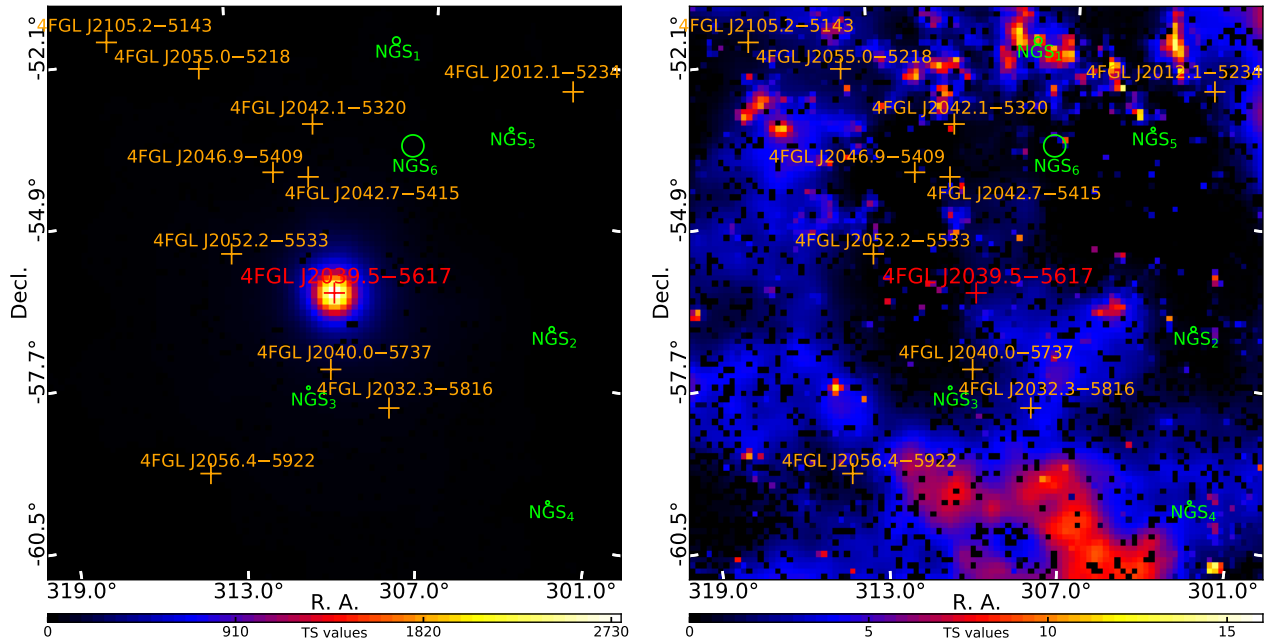


Figure 1. 0.1–500.0 GeV TS maps centered on 4FGL J2039.5–5617 with a region of $10^\circ \times 10^\circ$. The target is marked by a red cross, while other γ -ray sources from the 4FGL catalog are denoted by orange crosses, the six NGSs are shown as green circles, with radii proportional to their positional uncertainties. Left panel: TS map showing the γ -ray emissions from 4FGL J2039.5–5617, derived from the best-fit model with the target excluded. Right panel: Residual TS map generated using the same model, but including 4FGL J2039.5–5617.

ated two TS maps for 4FGL J2039.5–5617, as shown in Figure 1. The left panel displays the γ -ray emissions from 4FGL J2039.5–5617, and the right panel shows the residual γ -rays after excluding emissions from all sources in the best-fit model. In the residual map, the maximum TS value among all pixels is ~ 13.5 . The best-fit results for the target, labeled “Whole”, are summarized in Table 1 and shown in Figure 2 with a black solid line. While the results for the six NGSs are presented in Table 2. These results indicate that the γ -ray emissions from 4FGL J2039.5–5617 are better described by the PLE4 model, and subsequent data analysis was conducted based on the best-fit model.

2.2. Spectral Analysis

For the spectral analysis, we used Fermi-LAT events in the 0.1–500.0 GeV energy range. The spectral energy distribution (SED) of 4FGL J2039.5–5617 was extracted by dividing this range into 15 equally logarithmically spaced energy bins, and a binned likelihood analysis was performed in each bin to derive the γ -ray flux. In this procedure, only the normalization parameters of γ -ray sources within 5° of the target were left free, while all other parameters were fixed to the values obtained from the new model file. For energy bins with TS values ≥ 4 , the fluxes are shown as black data points in Figure 2, whereas for bins with TS < 4 , 95% flux upper

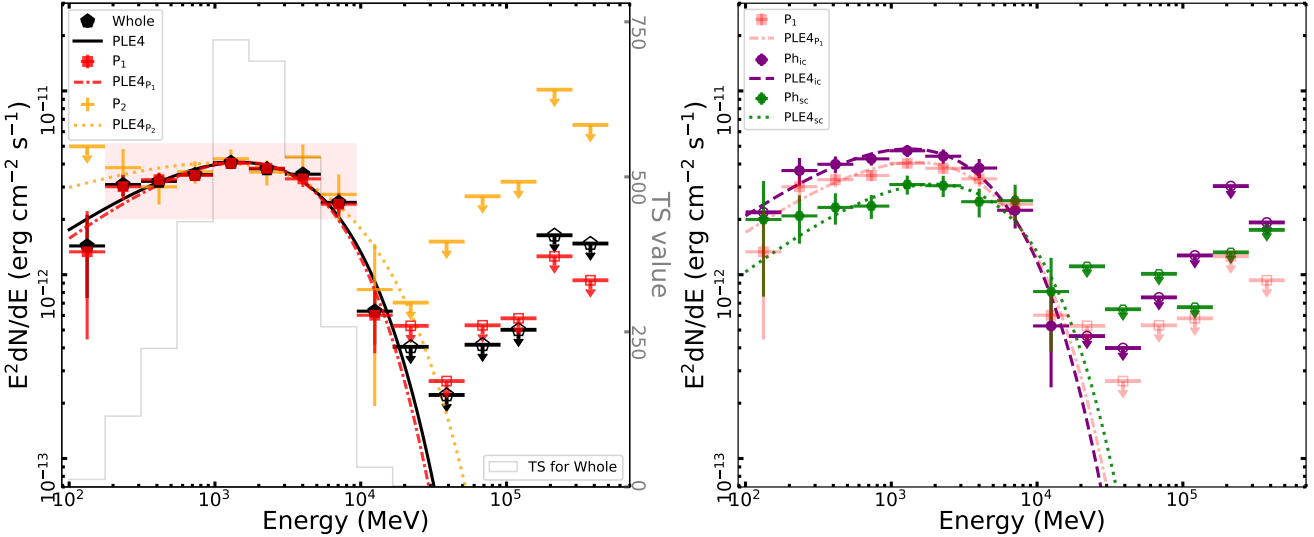


Figure 2. SEDs of 4FGL J2039.5–5617 in 0.1–500.0 GeV. Left: SEDs for three time intervals, 2008–08–04 to 2024–10–23 (black, Whole), 2008–08–04 to 2021–08–01 (red, P_1), and 2021–08–01 to 2024–10–23 (orange, P_2), with their best-fit PLE4 models shown as a black solid, red dashed-dotted, and orange dotted line, respectively. For the Whole results, TS values for each energy bin are displayed as a gray histogram (on right y-axis). Right: SEDs during the epoch where the AP light curve shows periodicity (P_1). The red points match those in the left panel, while purple and green points correspond to phase intervals around inferior and superior conjunction, respectively, as that indicated by the pink and cyan shaded regions in Figure 6. Their best-fit models are shown as purple dashed and green dotted lines, respectively.

limits are plotted. TS values for each energy bin are shown with a gray histogram on the right y-axis. As shown in Figure 2, the target is clearly significant in the 0.18–9.39 GeV range, where all bins have TS values > 100 . Accordingly, the subsequent timing analysis was primarily concentrated on this energy range.

2.3. Timing Analysis

To conduct a blind search for the orbital period of PSR J2039–5617 in the GeV, we applied a modified aperture photometry (AP) method to construct the light curve with a time bin of 500 s. To optimize the signal-to-noise ratio for detecting periodic signals, we focused on the energy range of 0.18–9.39 GeV, corresponding to the pink-shaded region in the SED, where the target is most significant. Testing different energy cuts could slightly increase the power of the detected peak, but we did not investigate how the power of the periodic signal depends on the energy range. For our timing analysis, events centered on 4FGL J2039.5–5617 within an aperture radius of 2.76° were selected, following the criteria established by Abdo et al. (2010b). Using *gtmktime*, we excluded periods when the target was within 5° of the Sun or Moon to eliminate their potential influence. To minimize the impact of significant exposure variations across time bins, exposures were calculated using *gtxposure*. Probabilities for each event, indicating their likelihood of originating from 4FGL J2039.5–5617, were assigned using *gtsrcprob* based on the new model file.

We then constructed the AP light curve, using the assigned probabilities as weights (Kerr 2011; Fermi LAT Collaboration et al. 2012; Corbet et al. 2019). Finally, the times of light curve were barycenter corrected using *gtbary*.

We used a common timing analysis tool, the Lomb–Scargle Periodogram (LSP), to obtain the power spectrum of the AP light curve (Lomb 1976; Scargle 1982; Zechmeister & Kürster 2009). Compared to other algorithms, the LSP is highly effective in detecting periodic signals in unevenly sampled data. It handles noisy data well, is computationally efficient, and provides clear and reliable results for identifying and analyzing periodicities. We searched for periodic signals within a frequency range of $f_{\min} = 0.01$ to $f_{\max} = 10$ day $^{-1}$ with a frequency resolution of $\delta f = 1/T_{\text{obs}}$, where $T_{\text{obs}} \sim 5924.268$ day is the duration of Fermi-LAT observations. The number of independent frequencies (the trial factor) was calculated as $N = (f_{\max} - f_{\min})/\delta f = 59,183$. To be conservative, we adopted this trial numbers for all subsequent timing analyses. The LSP results are shown in the left panel of Figure 3. A distinct power peak, with a power value of ~ 17.64 , was observed around the orbital period reported in previous literatures (Salvetti et al. 2015; Ng et al. 2018; Clark et al. 2021; Corongiu et al. 2021). We determined that the probability (p_{lsp}) of obtaining this power level due to random fluctuations (Gaussian white noise) is approximately 2.17×10^{-8} (Lomb 1976; Scargle 1982). After ac-

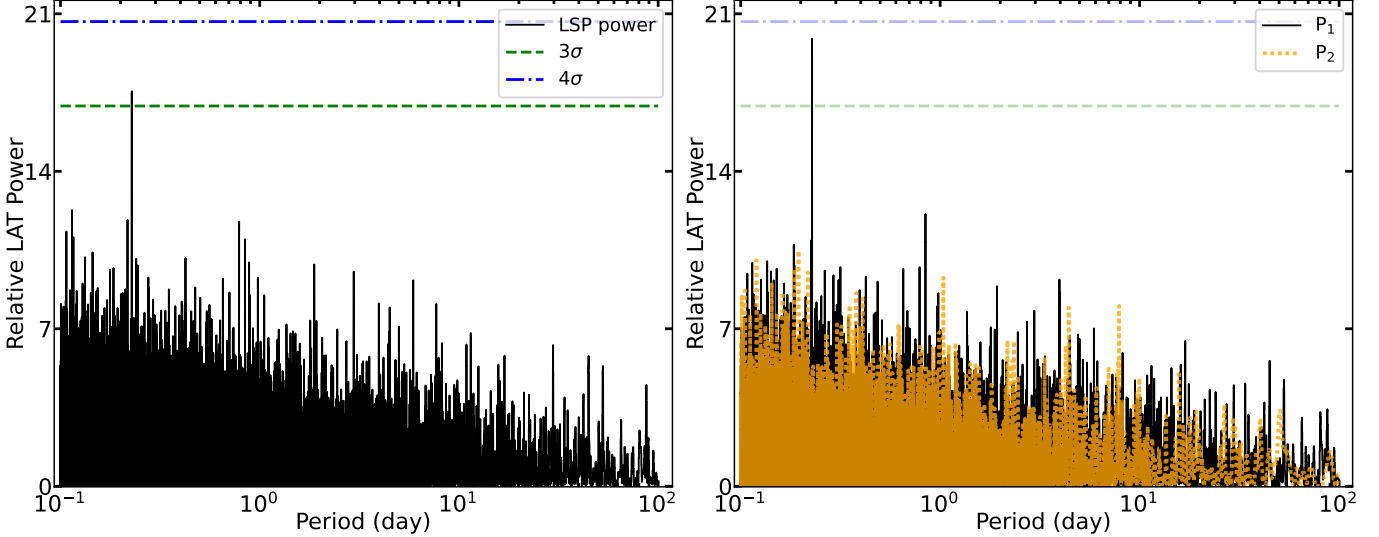


Figure 3. LSP power spectra (black histogram) of 4FGL J2039.5–5617 derived from the AP light curve in 0.18–9.39 GeV. Left: LSP power spectrum for the Whole AP light curve, with the 3σ and 4σ confidence levels indicated by green dashed and blue dash-dotted lines, respectively. Right: LSP power spectra for the AP light curve in P_1 and P_2 , shown in black and orange, respectively.

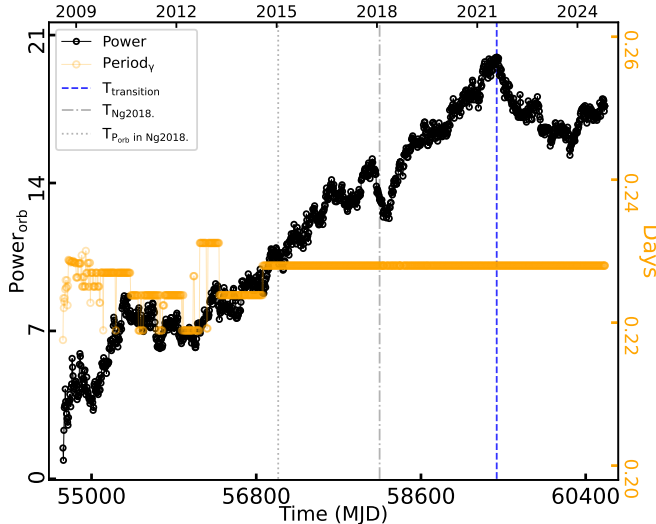


Figure 4. LSP power values around the periodic signal obtained from the accumulated data. The time axis corresponds to the end dates of the AP light curves, all starting from the same epoch (MJD 54682.687). As an example, the AP light curve spanning from 2008 August 4 to 2021 August 1 yields the highest LSP power of ~ 19.95 (blue dashed line). The gray dashed-dotted line indicates the end date of the dataset analyzed by Ng2018, while the gray dotted line marks the epoch when orbital modulation was reported to disappear in their work. In comparison, the blue dashed line denotes the epoch at which we find the modulation to vanish. The evolution of the signal period with accumulated data is plotted as orange circles on the right y-axis.

counting for the number of trials N , we calculated a false alarm probability (FAP) to be $FAP = 1 - (1 - p_{\text{LSP}})^N \sim N \times p_{\text{LSP}} = 1.28 \times 10^{-3}$, corresponding to a confidence

level of 3.2σ . In Figure 3, we also show 3σ and 4σ confidence levels with green dashed and blue dashed-dotted lines, respectively.

Considering the orbital modulation transitions in γ -rays for the Redback system, as reported by Ng2018 and Corbet et al. (2022), we analyzed the time-dependent variations in the power values of this periodic signal. The power values are shown as black circles in Figure 4. Additionally, the temporal changes in the period of the orbital modulation are colored in orange on the right side of Figure 4. As shown in the figure, the orbital modulation transition occurs at 2021 August 1 (MJD 59427.683, defined as $T_{\text{transition}}$), marked by a blue dashed line. Based on this transition, we divided the Fermi-LAT observations into two segments: data prior to $T_{\text{transition}}$ is designated as Part 1 (P_1), and data after $T_{\text{transition}}$ as Part 2 (P_2).

Therefore, we divided the AP light curve into two parts with using the division time of $T_{\text{transition}}$, and generated their power spectra using the same timing analysis process, they are displayed in the right panel of Figure 3. For P_1 (the black solid histogram), the orbital signal power rises to ~ 19.95 , with a FAP of $\sim 1.27 \times 10^{-4}$, corresponding to a 3.8σ confidence level, based on the previous estimation method. And its period is $P_{\text{orb}} = 0.2279781(9)$ days, where the uncertainties were calculated by $\delta P = \frac{3}{8} \frac{P^2}{T_{\text{obs}} \sqrt{p_n}}$ (Corbet et al. 2022). In contrast, for P_2 (orange dashed histogram), the orbital modulation signal has completely disappeared. Our results show some discrepancies compared to those reported by Ng2018.

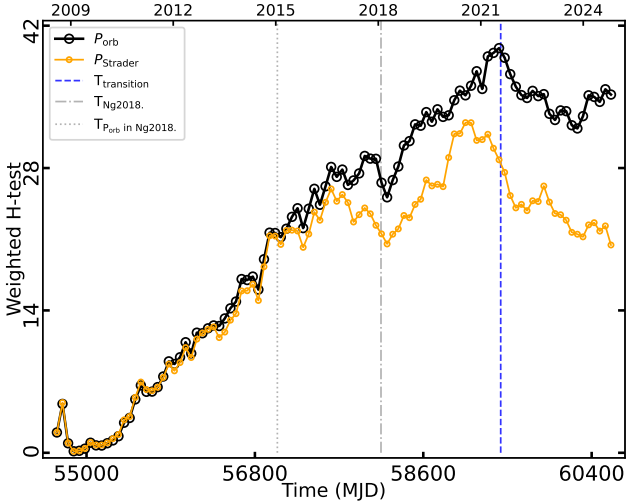


Figure 5. Cumulative H-test results obtained using the orbital periods P_{orb} (derived in this work, black) and P_{Strader} (adopted by Ng2018, orange). All others are the same as in Figure 4.

To further investigate the reasons for the discrepancy, we employed the H-test method, which is a statistical test similar to the Rayleigh test, to our data. The results are shown in Figure 5. We performed the H-test using both the orbital period of P_{orb} and P_{Strader} ($=0.2279817$ days) that adopted by Ng2018. As shown in Figure 5, the difference between this two results begins to increase gradually around MJD 57040 (gray dotted line).

We speculate that this difference mainly arises from the use of different orbital periods. When the adopted orbital period deviates from the true value, the impact of this deviation on the results is relatively small in the early stage of observation (e.g., before MJD 57040). However, as time progresses, the cumulative error in the orbital period increases, resulting in a more significant effect on the results in the later stage (after MJD 57040). In addition, compared with Ng2018, we used updated Fermi-LAT data and an improved version of Fermi-Tools. And the 4FGL-DR3 also includes several newly identified γ -ray sources (e.g., 4FGL J2046.9+5409), and the nearby source, 3FGL J2051.8-5535, also exhibited a γ -ray flare around MJD 57040 (see the Figure 9 in Ng2018). These factors may have increased the probability of misidentifying non-target γ -rays as originating from the target. Such non-target γ -rays, which are not modulated, could weaken the significance of the periodic signal in the data, thereby contributing to the differences in this timing results between ours and Ng2018.

Based on P_{orb} , the H-test results show that the periodic signal reaches its maximum at MJD 59409.865 (around $T_{\text{transition}}$), which is consistent with the LSP

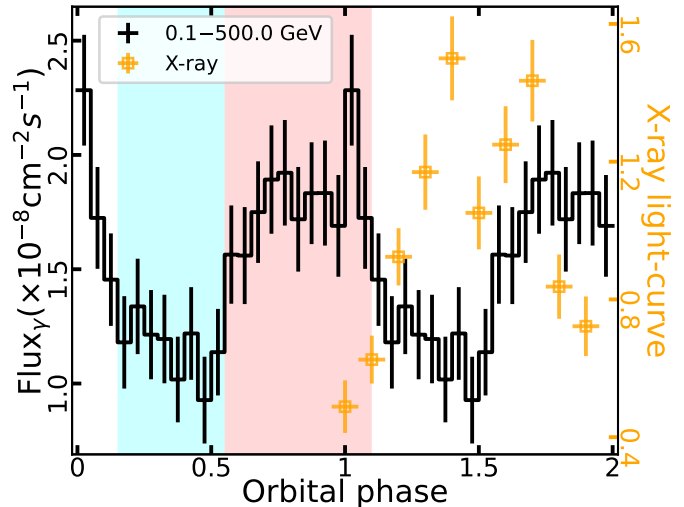


Figure 6. Phase-resolved light curves derived from the 0.1–500.0 GeV Fermi-LAT events in P_1 , folded over the γ -ray orbital period of 0.2279781 days. The phase intervals around the inferior and superior conjunctions are indicated by the pink and cyan shades. The orange data points (right y-axis) show the schematic X-ray modulation profile of the counterpart to PSR J2039–5617, adapted from Salvetti et al. (2015).

results. The H-test value for the whole data is 35.22, corresponding to a p -value of $\sim 7.61 \times 10^{-7}$ (5.0σ). And the maximum H-test value is 39.79, has a p -value of $\sim 1.22 \times 10^{-7}$ (5.3σ). When calculated H-test results using the period of P_{Strader} , the signal becomes similar to that reported by Ng2018 over the same time interval.

We then performed likelihood analysis separately on each of these two data segments, and the results are summarized in Table 1, labeled as P_1 and P_2 , respectively. We also created their SEDs and show them in left panel of Figure 2. From these results, we observe that the spectral shape of the target shows no significant differences between the two segments.

2.4. Phase-resolved Analysis

To investigate the γ -ray orbital modulation profile of PSR J2039–5617, we performed a likelihood analysis on the phase-resolved Fermi-LAT data, adopting its orbital period of P_{orb} in the 0.1–500 GeV energy range. The resulting phase-resolved likelihood light curve is presented in Figure 6. These results clearly show that the γ -ray flux of PSR J2039–5617 is modulated by its orbital period. The modulation profile exhibits a rapid rise followed by a gradual decline, and a possible structure with two asymmetric peaks was detected in the phase-resolved light curve.

To explore potential variations in the γ -ray spectral properties across different orbital phases, we derived the SEDs around the inferior and superior conjunctions, cor-

responding to phase ranges of 0.55–1.1 (denoted as Ph_{ic}) and 0.15–0.55 (Ph_{sc}), respectively. A likelihood analysis was performed on events within these two phase ranges, with the best-fit parameters summarized in Table 1. Based on these fits, the SEDs were constructed and are shown in the right panel of Figure 2, in purple and green, respectively. The results indicate that, aside from a significant flux difference at lower energies (in \sim 0.1–5.3 GeV), the spectral shapes show no noticeable differences between the two orbital states.

To facilitate the comparison of the modulation profiles between γ -rays and X-rays, we extracted the schematic X-ray modulation profile of the counterpart to PSR J2039–5617 from Figure 3 of Salvetti et al. (2015) and replotted it in Figure 6 using the orange data points on the right y-axis. It can be seen that the modulation profiles of γ -rays and X-rays appear to be offset by \sim 0.5 in phase.

3. SUMMARY AND DISCUSSION

PSR J2039–5617 is a redback MSP binary system, consisting of a compact star with a mass of 1.1–1.6 M_{\odot} and a low-mass companion of 0.15–0.22 M_{\odot} (Clark et al. 2021; Corongiu et al. 2021). Salvetti et al. (2015) first identified its orbital period of 0.2245 days from both X-ray and optical observations. Then Ng2018 reported an evidence of γ -ray orbital modulation from 2008 August 4 to 2015 January 18, they also provided a detailed discussion for the γ -ray emissions from this binary system. In this work, we extend the analysis to Fermi-LAT data spanning from 2008 August 4 to 2024 October 23. Our results confirm the orbital period at 0.2279781 days and suggest that the modulation persists longer than previously reported, disappearing around 2021 August. The observational time span over which the orbital period of PSR J2039–5617 was detected is approximately twice as long as that reported by Ng2018.

A comparison between our results and those of Ng2018 highlights an interesting discrepancy in the reported significance of the orbital period signal. While Ng2018 found a $\sim 4\sigma$ confidence level, our analysis, despite being based on nearly twice as much data, yields a similar significance. One possible explanation lies in the different statistical methods adopted, Ng2018 employed the Rayleigh test, whereas we applied the LSP. Alternatively, the discrepancy may arise from differences in how trial factors were handled in our analysis, as including a larger number of trials naturally reduces the estimated significance. When applying an H-test approach similar to that adopted by Ng2018, the signal significance increased to 5.3σ . This suggests that the robustness of the periodic signal detection is highly sensitive to both

the choice of statistical method and the treatment of trial corrections.

A comparison between our Figure 6 and the γ -ray folded light curves presented in Ng2018 (i.e., their Figures 4 and 5) reveals clear differences between the results obtained from photon folding and those derived from likelihood analysis when constructing the phase-resolved light curve. Similar conclusions are observed in other cases we examined (Zhang et al., in preparation). From experience with data analysis, the likelihood-based approach is generally more reliable for certain binaries, particularly for relatively faint γ -ray sources. While for very bright γ -ray binaries, such as LS 5039 (Abdo et al. 2009a), LS I +61 303 (Abdo et al. 2009b), and 1FGL J1018.6–5856 (Corbet et al. 2016) the two methods are expected to yield results that are largely consistent. Another possible explanation lies in the difference in data volume mentioned above: Ng2018 used only about six years of data to construct the folded light curve, whereas our phase-resolved analysis is based on \sim 13 years of data, nearly doubling the dataset compared with theirs.

The phase-resolved results around the superior (indicated by the cyan shade in Figure 6) and inferior (shown in pink) conjunctions indicate that the γ -ray spectra of the source remain nearly unchanged, with only the flux varying in 0.1–5.3 GeV, likely due to geometric factors. If the γ -ray emission mechanism is based on the IC scattering between the pulsar wind and the stellar soft photons, this suggests that the soft photon density around the stellar and the relativistic charged particles from the pulsar wind in the emitting region remain stable. Therefore, the spectral properties of the γ -ray emissions do not modulate with the orbital phase. The phase-resolved light curve further shows that the target emits γ -rays throughout the entire orbital phase, suggesting that the γ -ray emission region in the IC model has a significantly larger extent, meaning that the emission is spread out over a wide area rather than being concentrated in a narrow beam. This larger emission region allows an observer to detect the emission in any geometric configuration. From this perspective, it also resembles the γ -ray magnetosphere radiation mechanism in pulsars (Ravi et al. 2010).

The observed phase relationship between the X-ray and γ -ray modulations provides important insight into the emission geometry of this system. While γ -ray maxima are typically associated with inferior conjunction of orbital phase (when the companion star passes in front of the pulsar from the observer’s perspective) and X-ray maxima with superior conjunction, the limited observational coverage prevents us from establishing the precise

orbital phases for the target. Nevertheless, the ~ 0.5 phase offset between the γ -ray and X-ray light curves (shown in Figure 6) is consistent with the expected anti-correlation predicted by theoretical models of IC scattering and relativistic Doppler boosting in compact binaries. This agreement supports the interpretation that the observed high-energy radiation arises from the interplay between these mechanisms. This anti-correlated behavior between γ -rays and X-rays has been reported in numerous Redback and Black Widow pulsars, including the recent case reported by Sim et al. (2024), as well as in γ -ray binaries (Corbet et al. 2016, 2019). Our results therefore not only align with these earlier studies but also extend the observational evidence to this newly examined source. Conducting detailed phase-resolved analyses will be critical to tightly constrain the orbital geometry and to assess whether the source conforms to the canonical phenomenology of Redback and Black Widow pulsars.

Since we expect the γ -ray orbital modulation to originate from the geometric configuration of IC scattering, the modulation profile is typically anticipated to exhibit a symmetric single-peak structure (Wu et al. 2012). However, the phase-resolved light curve of PSR J2039–5617 reveals a possible structure with two asymmetric peaks. Currently, the statistical significance is still insufficient for an in-depth discussion. Future Fermi-LAT observations, with larger datasets, may provide the necessary data to either confirm or refute the presence of this structure, thereby offering valuable insights into the emission mechanisms operating in spider pulsar systems.

Last but not least, we know that the disappearance of periodic modulation may mark a critical phase in the evolution of compact binaries, possibly corresponding to the transition from a rotation-powered MSP state to an accretion-powered LMXB state. We observed that, prior to 2021 August, the γ -ray orbital modulation persisted, suggesting that PSR J2039–5617 was in the MSP state during this period. Subsequently, the system transitioned to the LMXB state, where the accretion process became dominant, forming an accretion disk, disrupting the IBS, and preventing particles from acquiring sufficient energy. This disruption in the IC scattering between the pulsar and its companion star led to the interruption of orbital modulation in γ -rays. However, current observational evidence is insufficient to confirm this scenario. To validate it, additional observational data are required, particularly optical and/or X-ray data, to compare with previous observations and investigate the presence of an accretion disk as well as variations in the X-ray luminosity of PSR J2039–5617. Nevertheless, although PSR J2039–5617 may not have transitioned to an LMXB state, some changes in the system did occur.

¹ We would like to thank the anonymous referee for the helpful suggestions. This work was partially supported by the National Natural Science Foundation of China under grant Nos. 12233006, 12163006, and 12103046, and by the Scientific Research and Innovation Project of Postgraduate Students in the Academic Degree of Yunnan University Nos. KC-242410143 and KC-252512090. P.Z. and S.C. acknowledge support from the Xingdian Talent Support Plan - Youth Project.

REFERENCES

Abdo, A. A., Ackermann, M., Ajello, M., et al. 2009a, ApJL, 706, L56, doi: [10.1088/0004-637X/706/1/L56](https://doi.org/10.1088/0004-637X/706/1/L56)
 —. 2009b, ApJL, 701, L123, doi: [10.1088/0004-637X/701/2/L123](https://doi.org/10.1088/0004-637X/701/2/L123)
 —. 2010a, ApJS, 188, 405, doi: [10.1088/0067-0049/188/2/405](https://doi.org/10.1088/0067-0049/188/2/405)
 —. 2010b, ApJ, 708, 1254, doi: [10.1088/0004-637X/708/2/1254](https://doi.org/10.1088/0004-637X/708/2/1254)
 Acero, F., Ackermann, M., Ajello, M., et al. 2015, ApJS, 218, 23, doi: [10.1088/0067-0049/218/2/23](https://doi.org/10.1088/0067-0049/218/2/23)
 Alpar, M. A., Cheng, A. F., Ruderman, M. A., & Shaham, J. 1982, Nature, 300, 728, doi: [10.1038/300728a0](https://doi.org/10.1038/300728a0)
 Archibald, A. M., Stairs, I. H., Ransom, S. M., et al. 2009, Science, 324, 1411, doi: [10.1126/science.1172740](https://doi.org/10.1126/science.1172740)
 Ballet, J., Bruel, P., Burnett, T. H., Lott, B., & The Fermi-LAT collaboration. 2023, arXiv e-prints, arXiv:2307.12546, doi: [10.48550/arXiv.2307.12546](https://doi.org/10.48550/arXiv.2307.12546)
 Benvenuto, O. G., De Vito, M. A., & Horvath, J. E. 2014, ApJL, 786, L7, doi: [10.1088/2041-8205/786/1/L7](https://doi.org/10.1088/2041-8205/786/1/L7)
 Bhattacharya, D., & van den Heuvel, E. P. J. 1991, PhR, 203, 1, doi: [10.1016/0370-1573\(91\)90064-S](https://doi.org/10.1016/0370-1573(91)90064-S)
 Chen, H.-L., Chen, X., Tauris, T. M., & Han, Z. 2013, ApJ, 775, 27, doi: [10.1088/0004-637X/775/1/27](https://doi.org/10.1088/0004-637X/775/1/27)
 Clark, C. J., Nieder, L., Voisin, G., et al. 2021, MNRAS, 502, 915, doi: [10.1093/mnras/staa3484](https://doi.org/10.1093/mnras/staa3484)
 Corbet, R. H. D., Chomiuk, L., Coe, M. J., et al. 2016, ApJ, 829, 105, doi: [10.3847/0004-637X/829/2/105](https://doi.org/10.3847/0004-637X/829/2/105)
 —. 2019, ApJ, 884, 93, doi: [10.3847/1538-4357/ab3e32](https://doi.org/10.3847/1538-4357/ab3e32)
 Corbet, R. H. D., Chomiuk, L., Coley, J. B., et al. 2022, ApJ, 935, 2, doi: [10.3847/1538-4357/ac6fe2](https://doi.org/10.3847/1538-4357/ac6fe2)

Corongiu, A., Mignani, R. P., Seyffert, A. S., et al. 2021, *MNRAS*, 502, 935, doi: [10.1093/mnras/staa3463](https://doi.org/10.1093/mnras/staa3463)

Fermi LAT Collaboration, Ackermann, M., Ajello, M., et al. 2012, *Science*, 335, 189, doi: [10.1126/science.1213974](https://doi.org/10.1126/science.1213974)

Fruchter, A. S., Stinebring, D. R., & Taylor, J. H. 1988, *Nature*, 333, 237, doi: [10.1038/333237a0](https://doi.org/10.1038/333237a0)

Kerr, M. 2011, *ApJ*, 732, 38, doi: [10.1088/0004-637X/732/1/38](https://doi.org/10.1088/0004-637X/732/1/38)

Lomb, N. R. 1976, *Ap&SS*, 39, 447, doi: [10.1007/BF00648343](https://doi.org/10.1007/BF00648343)

Ng, C. W., Takata, J., Strader, J., Li, K. L., & Cheng, K. S. 2018, *ApJ*, 867, 90, doi: [10.3847/1538-4357/aae308](https://doi.org/10.3847/1538-4357/aae308)

Nolan, P. L., Abdo, A. A., Ackermann, M., et al. 2012, *ApJS*, 199, 31, doi: [10.1088/0067-0049/199/2/31](https://doi.org/10.1088/0067-0049/199/2/31)

Ravi, V., Manchester, R. N., & Hobbs, G. 2010, *ApJL*, 716, L85, doi: [10.1088/2041-8205/716/1/L85](https://doi.org/10.1088/2041-8205/716/1/L85)

Roberts, M. S. E. 2013, in IAU Symposium, Vol. 291, *Neutron Stars and Pulsars: Challenges and Opportunities after 80 years*, ed. J. van Leeuwen, 127–132, doi: [10.1017/S174392131202337X](https://doi.org/10.1017/S174392131202337X)

Salvetti, D., Mignani, R. P., De Luca, A., et al. 2015, *ApJ*, 814, 88, doi: [10.1088/0004-637X/814/2/88](https://doi.org/10.1088/0004-637X/814/2/88)

Scargle, J. D. 1982, *ApJ*, 263, 835, doi: [10.1086/160554](https://doi.org/10.1086/160554)

Sim, M., An, H., & Wadiasingh, Z. 2024, *ApJ*, 964, 109, doi: [10.3847/1538-4357/ad25fb](https://doi.org/10.3847/1538-4357/ad25fb)

Wu, E. M. H., Takata, J., Cheng, K. S., et al. 2012, *ApJ*, 761, 181, doi: [10.1088/0004-637X/761/2/181](https://doi.org/10.1088/0004-637X/761/2/181)

Zechmeister, M., & Kürster, M. 2009, *A&A*, 496, 577, doi: [10.1051/0004-6361:200811296](https://doi.org/10.1051/0004-6361:200811296)